THE UNIVERSITY *of* EDINBURGH

Edinburgh Research Explorer

Propagator and wave-equation inversion for near-receiver material properties

OPEN ACCESS

Propagator and wave-equation inversion for near-receiver material properties

R. van Vossen,[1] J. Trampert[1] and A. Curtis[2,3]

[1]*Faculty of Earth Sciences, Utrecht University, Utrecht, the Netherlands. E-mail: vossen@geo.uu.nl*
[2]*Schlumberger Cambridge Research, High Cross, Cambridge, UK*
[3]*School of GeoSciences, Edinburgh University, Edinburgh, UK*

SUMMARY

Near-receiver material properties are required for the separation of the recorded wavefield into upgoing and downgoing *P* and *S* waves, and are also important for static time-shift corrections. However, it is difficult, especially in land seismics, to obtain reliable estimates for these local material properties using conventional techniques. We compare three methods for estimating these material properties using a 3-D geophone configuration. The first two methods are based on inversion of the wave equation and can be used on almost all of the recorded wavefield. However, they require that the wavefield is recorded by a dense 3-D receiver group to allow the computation of either spatial wavefield derivatives or interpolants. The third approach is based on the inversion of the vertical wavefield propagator. We present a procedure for estimating this propagator using only two multicomponent geophones, one buried and one positioned at the surface. Propagator estimation and inversion avoids the explicit computation of wavefield derivatives, and is therefore less sensitive to measurement errors than both wave-equation inversion schemes. However, in the form presented it requires the identification of arrivals of incoming waves that are isolated in time, and can only be applied to such data. Noise tests demonstrate that the propagator inversion provides accurate estimates for *P*- and *S*-wave velocities of a near-surface low-velocity layer, and is robust with respect to signal-generated near-surface reverberations. In case of a near-surface velocity gradient, velocities are obtained which are consistent with effective medium velocities.

Key words: land seismics, multicomponent, near-surface, propagator, wave equation, waveform inversion.

1 INTRODUCTION

Most observations of seismic waves are made either at, or very near to, the Earth's surface. Before reliable subsurface information can be retrieved from these recordings, corrections are required for local near-receiver structure, since variations in this structure often cause data perturbations of a similar magnitude to the target signal (e.g. Goupillaud 1961). The variability of the elastic properties close to the measurement surface is due to a variety of geological processes and petrophysical properties, among them porosity, permeability, fractures, the presence of fluids in pores, compaction, diagenesis and metamorphism (Toksöz *et al.* 1976).

Variations in near-receiver elastic properties cause the following complications. First, receiver static variations in the data are receiver-to-receiver traveltime anomalies which occur due to the propagation of most of the seismic energy through the heterogeneous shallow structure. Secondly, poor repeatability of the source signature and changes in the source radiation pattern are also attributed to lateral changes in near-surface material properties (Aritman 2001). Thirdly, lateral variations in free-surface reflectivity cause differences in the amount of reflected and converted energy. This results in amplitude perturbations, especially on horizontal recordings (Kähler & Meissner 1983). Decomposing the recorded wavefield into upgoing and downgoing *P* and *S* waves allows an analysis of these wavefields without the effects of any free-surface interaction (e.g. Dankbaar 1985; Wapenaar *et al.* 1990). However, to perform wavefield decomposition the free-surface reflectivity, and hence local subreceiver properties, need to be known.

Since conventional seismic data are acquired only at the surface, the problem of determining seismic subsurface properties is ill-posed. Curtis & Robertsson (2002) therefore proposed to use dense 3-D recording patterns to better constrain land seismic near-surface velocities. The pattern consists of a single buried three-component geophone and several surface geophones. The receivers are sufficiently close that spatial wavefield derivatives can be computed. These derivatives are required to invert the equation of motion for local material parameters.

Robertsson & Muyzert (1999) originally introduced this recording geometry to accomplish P/S separation by explicitly computing the divergence and the curl of the wavefield.

In other research fields, e.g. medical imaging, several concepts to estimate local material properties have been developed. Medical practitioners aim to estimate local material properties since variations in the mechanical properties of tissue often reflect early stage pathology (Gao *et al.* 1996). Unlike in conventional seismic surveys, the displacement field is measured throughout a tissue using measurement techniques based on ultrasound or magnetic resonance imaging (MRI) (Muthupillai *et al.* 1995). Quantitative elasticity reconstruction is achieved either by comparing modelled stress to measured strain (Gao *et al.* 1996; Van Houten *et al.* 1999) or by direct inversion of the observed displacement field. For example, Romano *et al.* (1998) and Oliphant *et al.* (1999, 2001) have shown that elastic properties can be estimated by localized inversion of the equation of motion.

We propose an alternative method to estimate local near-surface P- and S-wave velocities. This method was originally proposed by Trampert *et al.* (1993) to estimate the S-wave velocity structure and the quality factor in a borehole. This was achieved by estimating and inverting the vertical SH wavefield propagator derived from the spectral ratio of a downhole data record over a surface data record. We formulate this approach for the elastic P–SV case and a strategy for inverting the propagator for near-surface P- and S-wave velocities is developed.

Before discussing propagator estimation and inversion, we briefly review techniques based on direct inversion of the wave equation, including those from medical fields. For the purpose of comparison, we illustrate the importance of two of the methods and our propagator inversion method using signals perturbed by noise.

2 WAVE-EQUATION INVERSION

Oliphant *et al.* (1999, 2001) and Curtis & Robertsson (2002) proposed to constrain local material properties by algebraic inversion of the wave equation. A Cartesian coordinate system (x_1, x_2, x_3) is used with the positive vertical direction $z = x_3$ oriented downwards. The particle velocity is regarded as a function of space and time t, and is written as $\mathbf{v} = \mathbf{v}(\mathbf{x}, t)$. Overdots are used to indicate time derivatives (e.g. $\dot{\mathbf{v}} = \partial \mathbf{v}/\partial t$ and $\ddot{\mathbf{v}} = \partial^2 \mathbf{v}/\partial t^2$). The wave equation for $\mathbf{v}$ in a homogeneous, isotropic medium is then given by (Aki & Richards 2002):

$$\ddot{\mathbf{v}} = \alpha^2 \nabla(\nabla \cdot \mathbf{v}) - \beta^2 \nabla \times (\nabla \times \mathbf{v}), \tag{1}$$

where $\alpha = [(\lambda + 2\mu)/\rho]^{1/2}$ is the P-wave velocity, $\beta = (\mu/\rho)^{1/2}$ is the S-wave velocity, and λ and μ are the Lamé parameters. Derivative conditions can be derived from the constitutive equation and the free-surface boundary conditions. The constitutive equation for a homogeneous, elastic medium reads:

$$\dot{\sigma}_{ij} = \lambda \partial_k v_k \delta_{ij} + \mu(\partial_i v_j + \partial_j v_i), \tag{2}$$

where δ_{ij} is the Kronecker delta and ∂_k denotes the spatial derivative with respect to coordinate x_k. Boundary conditions state that the traction σ_{i3} vanishes at the free surface for $i = 1, 2, 3$, although in practice this is only an approximation, as air waves can exist. By setting $\sigma_{i3} = 0$ at the free surface, we can substitute for vertical wavefield derivative expressions with horizontal derivatives:

$$\partial_3 v_1 = -\partial_1 v_3, \tag{3}$$

$$\partial_3 v_2 = -\partial_2 v_3, \tag{4}$$

$$\partial_3 v_3 = -\left(\frac{\alpha^2 - 2\beta^2}{\alpha^2}\right)(\partial_1 v_1 + \partial_2 v_2). \tag{5}$$

Curtis & Robertsson (2002) showed that the following system of equations is obtained after substitution of the free-surface derivative conditions into the wave equation:

$$\ddot{v}_1 = \beta^2 A_1(t) - \alpha^{-2} \beta^4 B_1(t), \tag{6}$$

$$\ddot{v}_2 = \beta^2 A_2(t) - \alpha^{-2} \beta^4 B_2(t), \tag{7}$$

$$\ddot{v}_3 = \alpha^2 A_3(t) - \beta^2 B_3(t). \tag{8}$$

Expressions for the measurable coefficients A_i and B_i are given in Appendix A. These coefficients require the evaluation of spatial wavefield derivatives. A receiver group as illustrated in Fig. 1 allows the computation of these spatial and temporal derivatives using finite-difference operators (assuming that $v_2 = 0$ and $\partial_2 \mathbf{v} = \partial_{22} \mathbf{v} = \mathbf{0}$). The spatial derivatives can only be obtained accurately if the horizontal and vertical geophone spacings Δx and Δz satisfy the following criteria: $\Delta z \sim \lambda_z^{\min}/6$ and $\Delta x \sim \lambda_x^{\min}/6$, where $\lambda_x^{\min}$ and $\lambda_z^{\min}$ are the minimum effective wavelengths in the x or z direction, respectively (Levander 1988; Muijs *et al.* 2002). Assuming that these spatial derivatives can be calculated, eqs (6)–(8) can be inverted for α and β. The attractiveness of this method is that it can deal with the complete wavefield (Curtis & Robertsson 2002). On the other hand, it requires the computation of second-order derivatives which are likely to be affected by noise and measurement errors (Muijs *et al.* 2002).

Romano *et al.* (1998, 2000) suggested to transform the wave eq. (1) into an integral equation to avoid the computation of spatial wavefield derivatives. This approach is referred to as the variational formulation, and we present it for estimating local near-surface material properties
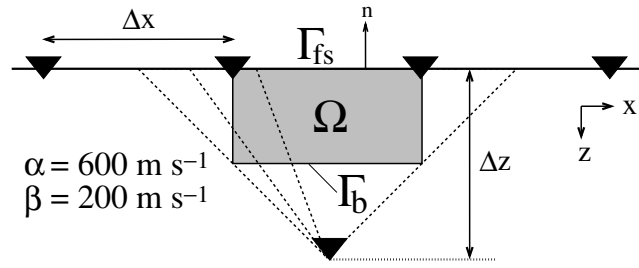
Figure 1. Geophone configuration for near-surface velocity estimation. The volume Ω bounded by surface $\Gamma = \Gamma_b \cup \Gamma_{fs}$ with outward-pointing normal vector **n** is used in the variational formulation. Wavefield interpolation is performed along the dashed lines.

using the geophone configuration shown in Fig. 1. Consider a vector-valued function **w** and a volume Ω bounded by a surface Γ with outward-pointing normal vector **n** (Fig. 1). In Appendix B, we demonstrate that eq. (1) is equivalent to

$$\int_\Omega d\Omega \mathbf{w} \cdot \ddot{\mathbf{v}} = \int_\Omega d\Omega \mathbf{v} \cdot \mathbf{w}_\Omega + \int_\Gamma d\Gamma \mathbf{n} \cdot \mathbf{w}_\Gamma, \tag{9}$$

where

$$\mathbf{w}_\Omega = \alpha^2 \nabla(\nabla \cdot \mathbf{w}) - \beta^2 \nabla \times (\nabla \times \mathbf{w}), \tag{10}$$

$$\mathbf{w}_\Gamma = (\alpha^2 - \beta^2)[\mathbf{w}(\nabla \cdot \mathbf{v}) - \mathbf{v}(\nabla \cdot \mathbf{w})] - \beta^2[\mathbf{v} \cdot (\nabla \mathbf{w})^T - \mathbf{w} \cdot (\nabla \mathbf{v})^T]. \tag{11}$$

Eq. (9) is known as Betti's theorem (Ben-Menahem & Singh 1981).

The surface $\Gamma = \Gamma_b \cup \Gamma_{fs}$, where Γ_{fs} is the surface of Ω which coincides with the free surface (see Fig. 1). Because the vector-valued function **w** can be chosen arbitrarily, boundary conditions can be imposed on **w** to aid the computation of the integrals in eq. (9). If we assume that

$$\mathbf{w} = \mathbf{0} \quad \text{on} \quad \Gamma_b \tag{12}$$

and

$$(\nabla \mathbf{w})^T \cdot \mathbf{n} = \mathbf{0} \quad \text{on} \quad \Gamma_b, \tag{13}$$

the contribution of the surface integral along Γ_b vanishes. The evaluation of the surface integral along Γ_{fs} requires the computation of first-order spatial wavefield derivatives at the free surface. These are also needed for accurate wavefield interpolation throughout Ω: first, the wavefield and its horizontal derivative are interpolated along the free surface using B-splines (Unser 1999). Secondly, the vector gradient of the wavefield is obtained using the free-surface conditions (eqs 3–5). Next, the wavefield in Ω is interpolated along lines from the surface to the buried geophone (the dashed lines in Fig. 1). The interpolated wavefield is parametrized by second-order polynomials, which are uniquely determined by the interpolated wavefield at the free surface, the directional derivative at the free surface and the wavefield at depth Δz. For sufficiently accurate wavefield interpolation within volume Ω, we found that, similar to the previous method, $\Delta z \sim \lambda_z^{\min}/6$ and $\Delta x \sim \lambda_x^{\min}/6$. Finally, the surface and volume integrals are evaluated using the trapezium rule.

Consider the following independent vector-valued functions:

$$\mathbf{w}_1 = (f_w, 0, 0)^T, \tag{14}$$

$$\mathbf{w}_2 = (0, 0, f_w)^T, \tag{15}$$

with

$$f_w(x_l, z_l) = \left(x_l^4 - 2x_l^2 + 1\right)(z_l - 1)^2. \tag{16}$$

The local coordinates x_l and z_l are related to x and z according to:

$$x_l = 2x/\Delta x_\Omega, \tag{17}$$

$$z_l = (2z - \Delta z_\Omega)/\Delta z_\Omega, \tag{18}$$

with Δx_Ω and Δz_Ω the lengths of the sides of volume Ω. The local coordinates are defined on the domain $x_l \in [-1, 1]$ and $z_l \in [-1, 1]$. The functions $\mathbf{w}_1$ and $\mathbf{w}_2$ satisfy the boundary conditions (eqs 12 and 13).

We illustrate both methods with a 2-D example. Synthetic data for a half-space model are computed using the Cagniard–de Hoop method (de Hoop & van der Hijden 1983). An explosive line source oriented in the x_2 direction is located at 200 m depth and emits a Ricker wavelet with a dominant frequency of 40 Hz. The P-wave velocity is 600 m s^{-1}, the S-wave velocity is 200 m s^{-1}, and the density is 1600 kg m^{-3}. Multicomponent geophones are centred around 50 m offset. The horizontal geophone spacing $\Delta x = 1.0$ m and the buried geophone is located at 0.50 m depth. For a Ricker wavelet with a 40 Hz dominant frequency, the maximum frequency $f_{\max}$ with significant energy is 80 Hz.
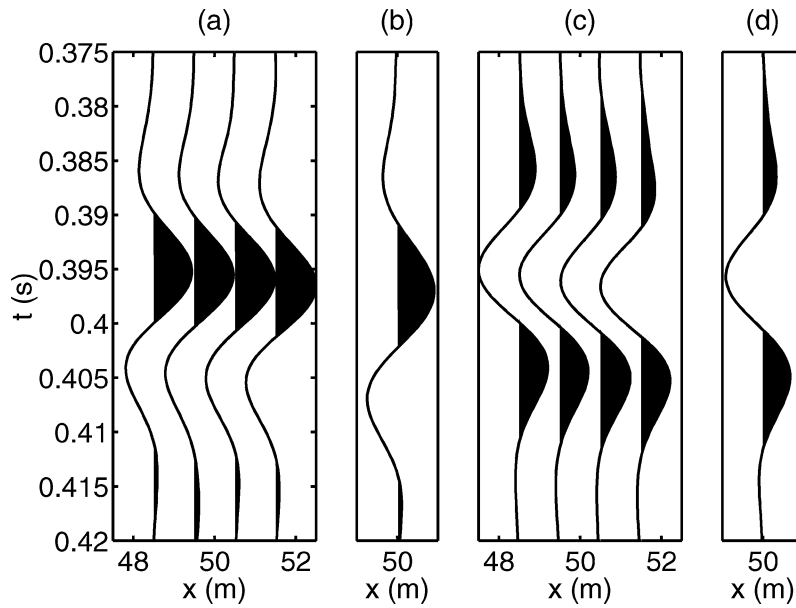
Figure 2. Synthetic data traces for (a) v_x at the surface, (b) v_x at depth Δz, (c) v_z at the surface and (d) v_z at depth Δz.
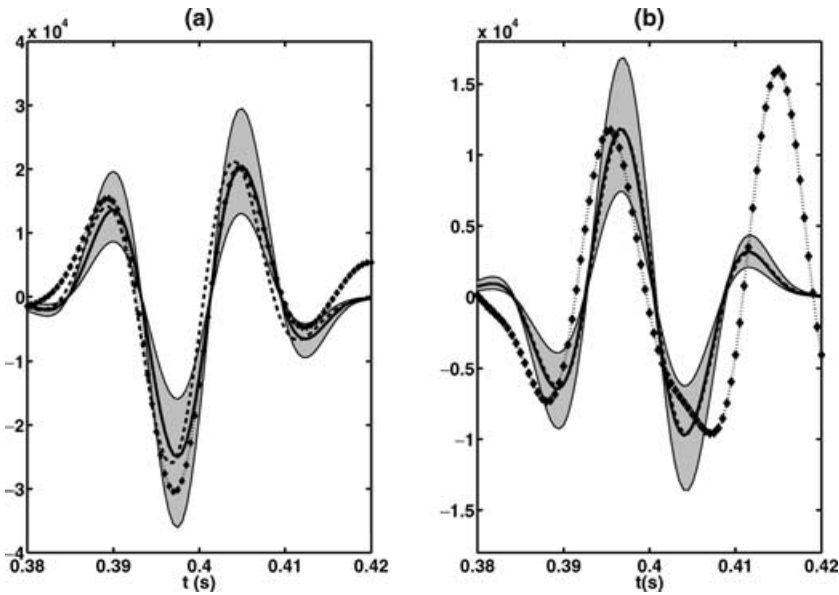

Figure 3. Sensitivity analysis for direct wave-equation inversion. (a) The waveforms of the left (dashed) and right side (solid line) of eq. (6), and the grey area illustrates the region for ± 20 per cent perturbations in β. The dotted line shows the effect of Gaussian noise (25 dB S/N ratio) added to the velocity recordings on the right side of eq. (6). Similarly, (b) shows the waveforms of eq. (8) and illustrates the region for ± 20 per cent perturbations in α. The dotted line shows the effect of Gaussian noise (25 dB S/N ratio) added to the velocity recordings.

Then, the minimum wavelength $\lambda_{min} = c_{min}/f_{max} = 2.5$ m, with c_{min} the minimum phase velocity. The geophone configuration satisfies the wavelength condition for the computation of derivatives and interpolants. The length of the sides of Ω are $\Delta x_\Omega = \Delta x$ and $\Delta z_\Omega = \Delta z/2$ (Fig. 1). Recorded data are shown in Fig. 2.

The constraints of direct wave-equation inversion on α and β are illustrated in Fig. 3. For the given model values α and β, there is a good match between the left and right side of eqs (6) and (8). For noise-free data, derivative operators are obtained sufficiently accurately with the geophone configuration of Fig. 1. Perturbing α or β results in amplitude changes in the waveforms of the right-side terms in eqs (6)–(8). We compare the sensitivity to perturbations in α and β with the effect of measurement errors in the particle velocity recordings. To study these effects, 25 dB uncorrelated Gaussian noise (peak-to-peak energy signal-to-noise (S/N) ratio) was added to the velocity recordings. A bandpass filter (20 Hz $< f <$ 100 Hz) was applied to these recordings before computing the wavefield derivatives. As a result, the effect of noise on temporal wavefield derivatives is reduced. However, spatial wavefield derivatives are still severely distorted by the added noise.
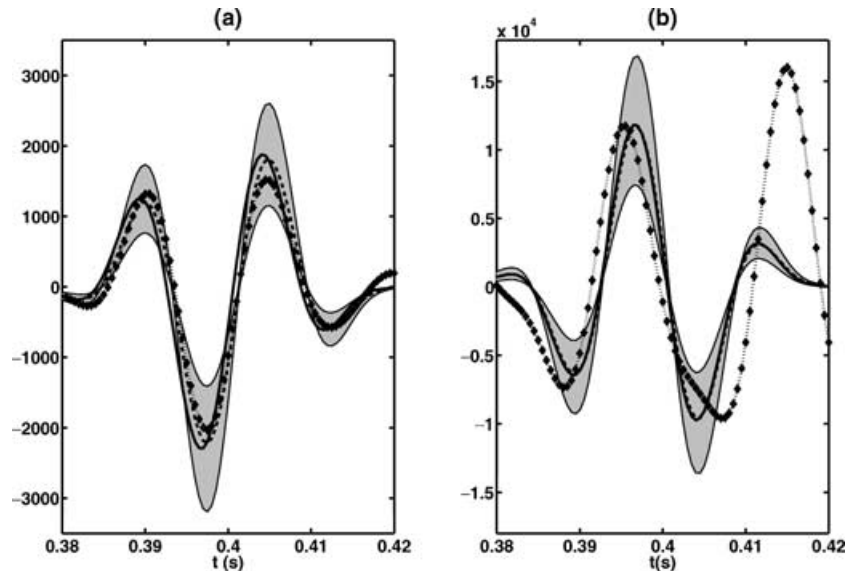
Figure 4. Sensitivity analysis for the variational formulation. The waveforms of the left (dashed) and right side (solid line) of eq. (9) are shown for $\mathbf{w}_1$ (a) and $\mathbf{w}_2$ (b). The grey area in (a) illustrates the region for $\pm$ 20 per cent perturbations in β, whereas (b) shows this region for $\pm$ 20 per cent perturbations in α. The dotted curves show the effect of Gaussian noise (25 dB S/N ratio) added to the velocity recordings.

Estimates for α are especially affected, since the wavelength for P waves is larger than for S waves. Consequently, the S/N ratio for spatial P-wave derivatives is lower than for S-wave derivatives.

Fig. 4 shows a similar analysis for the variational approach. There is a good agreement between the left and right side of equation (9) for the given model values α and β. In principle, the interpolation and integration steps are sufficiently accurate using the geophone configuration shown in Fig. 1. Perturbing α or β results in amplitude changes in the waveforms of the right side terms in eq. (9). A comparison between the sensitivity to α and β and the effects of noise (25 dB S/N ratio) shows that this approach is also very sensitive to the effects of noise, and again mostly for α.

These sensitivity tests demonstrate that it may only be possible to constrain β using these methods. There is not a clear difference between the derivative and variational formulation. However, for a geophone configuration with more than one buried geophone, an interpolation scheme can be developed which is less sensitive to random errors.

Muijs *et al.* (2002) studied the effect of deployment-related errors, such as misorientation and mislocation of geophones in a 3-D recording geometry, on the computation of divergence and curl. These are particularly sensitive to misorientations of geophones, requiring that the orientations of all geophones be accurate within $2°$.

Instead of using the full wave equation, the free-surface condition given in eq. (5) can be used to determine a velocity ratio between α and β (Curtis & Robertsson 2002). This only requires the computation of first-order spatial wavefield derivatives, and is therefore expected to be more robust than wave-equation inversion. Both the free-surface conditions and wave-equation inversion are applicable to the complete wavefield, except the airwave.

As an alternative, we propose a new method which avoids the explicit computation of spatial wavefield derivatives and imposes no requirements on the maximum depth separation of geophones. This is achieved by assuming that the incident wavefield can be described by a single plane wave.

3   PROPAGATOR ESTIMATION

Our alternative approach to wave-equation inversion is based on propagator inversion. Trampert *et al.* (1993) proposed estimating the S-wave velocity structure and the quality factor by analysing the vertical SH propagator in the time domain. The propagator contains all information on the material properties between the free surface and the depth of a buried geophone, and can be estimated directly from recorded data. The S velocity can be constrained by determining the time lag between the peaks in the SH propagator. This time difference represents the two-way traveltime of an SH wave to depth Δz. The amplitude difference between the peaks can be used to infer the quality factor: downward continuation of upgoing waves results in increasing amplitudes, whereas the amplitudes of downgoing waves decrease with depth.

We generalize this procedure to estimate the elastic P–SV propagator and illustrate a scheme to constrain near-surface P- and S-wave velocities based on waveform inversion of this P–SV propagator.

Assuming a plane wave solution for the wave equation, the plane wave at depth Δz can be written in the form

$$\mathbf{v}(t, x, \Delta z) = \mathbf{P}(t, x) * \mathbf{v}(t, x, 0), \tag{19}$$

where

$$\mathbf{P} = \begin{pmatrix} P_{11} & P_{12} & P_{13} \\ P_{21} & P_{22} & P_{23} \\ P_{31} & P_{32} & P_{33} \end{pmatrix} \tag{20}$$

and * denotes a temporal convolution. For a homogeneous, isotropic and elastic medium between the free surface and depth Δz, the propagator $\mathbf{P}$ is a function of the P-wave velocity α, the S-wave velocity β and the horizontal slowness p. For a free-surface incident plane wave with slowness p, the theoretical propagator coefficients read (Aki & Richards 2002):

$$\hat{P}_{11} = \beta^2 p^2 G_1^P + [(1 - 2\beta^2 p^2)/2]G_1^S, \tag{21}$$

$$\hat{P}_{22} = G_1^S, \tag{22}$$

$$\hat{P}_{33} = [(1 - 2\beta^2 p^2)/2]G_1^P + \beta^2 p^2 G_1^S, \tag{23}$$

$$\hat{P}_{13} = \left[p(1 - 2\beta^2 p^2)/(2q_P) \right] G_2^P - \beta^2 pq_S G_2^S, \tag{24}$$

$$\hat{P}_{31} = \beta^2 pq_P G_2^P - \left[p(1 - 2\beta^2 p^2)/(2q_S) \right] G_2^S, \tag{25}$$

$$\hat{P}_{12} = \hat{P}_{21} = \hat{P}_{23} = \hat{P}_{32} = 0, \tag{26}$$

where

$$G_1^P(t, p) = [\delta(t + q_P \Delta z) + \delta(t - q_P \Delta z)], \tag{27}$$

$$G_2^P(t, p) = [\delta(t + q_P \Delta z) - \delta(t - q_P \Delta z)], \tag{28}$$

$$G_1^S(t, p) = [\delta(t + q_S \Delta z) + \delta(t - q_S \Delta z)], \tag{29}$$

$$G_2^S(t, p) = [\delta(t + q_S \Delta z) - \delta(t - q_S \Delta z)]. \tag{30}$$

The vertical slownesses q_P and q_S are given by:

$$q_P = (\alpha^{-2} - p^2)^{1/2}, \tag{31}$$

$$q_S = (\beta^{-2} - p^2)^{1/2}. \tag{32}$$

Eqs (27)–(30) contain the phase shifts for two-way extrapolation of the wavefield towards depth Δz. Positive phase shifts describe the propagation of downgoing waves to Δz, whereas negative phase shifts indicate propagation of upgoing waves to this depth.

The coefficients of the propagator matrix (eqs 21–26) can be interpreted as follows. Extrapolation of P–SV waves is described by P_{11}, P_{13}, P_{31} and P_{33}, whereas for SH waves it is given by P_{22}. The amplitude terms before G_1^P, G_1^S, G_2^P and G_2^S are wavefield decomposition filters: the wavefield is separated into P, SV and SH waves before extrapolating the recordings to depth Δz, which is given by the phase terms. Finally, summation of the extrapolated decomposed wavefield renders the total wavefield at depth Δz (Osen *et al.* 1999; Aki & Richards 2002).

In the case of a non-attenuating medium, the extrapolation filters for elastic P–SV wave propagation can be obtained directly from the data by exploiting symmetry properties of the filters: the theoretical expressions for the extrapolation filters show that P_{11}, P_{22} and P_{33} are even functions around $t = 0$ and P_{13} and P_{31} are odd functions. Hence, the spectra of P_{11}, P_{22} and P_{33} are entirely real, whereas the spectra of P_{13} and P_{31} are purely imaginary. These properties are used to estimate the extrapolation filters without prior information on α, β and p. Equating real and imaginary parts of eq. (19) in the frequency domain shows that the propagator coefficients are given by:

$$P_{11} = \{\Re[v_3(\omega, x, 0)]\Re[v_1(\omega, x, \Delta z)] + \Im[v_3(\omega, x, 0)]\Im[v_1(\omega, x, \Delta z)]\}/D(\omega), \tag{33}$$

$$P_{33} = \{\Re[v_1(\omega, x, 0)]\Re[v_3(\omega, x, \Delta z)] + \Im[v_1(\omega, x, 0)]\Im[v_3(\omega, x, \Delta z)]\}/D(\omega), \tag{34}$$

$$P_{13} = i\{\Re[v_1(\omega, x, 0)]\Im[v_1(\omega, x, \Delta z)] - \Im[v_1(\omega, x, 0)]\Re[v_1(\omega, x, \Delta z)]\}/D(\omega), \tag{35}$$

$$P_{31} = i\{\Re[v_3(\omega, x, 0)]\Im[v_3(\omega, x, \Delta z)] - \Im[v_3(\omega, x, 0)]\Re[v_3(\omega, x, \Delta z)]\}/D(\omega), \tag{36}$$

where

$$D(\omega) = \Re[v_3(\omega, x, 0)]\Re[v_1(\omega, x, 0)] + \Im[v_3(\omega, x, 0)]\Im[v_1(\omega, x, 0)]. \tag{37}$$

In these equations, $\Re[v(\omega, x, z)]$ denotes the real part of $v(\omega, x, z)$ and $\Im[v(\omega, x, z)]$ is the imaginary part of $v(\omega, x, z)$. Expressions for $\mathbf{P}(t, x)$ are found by taking the inverse Fourier transform of eqs (33)–(36). Note that these symmetry properties break down for the P–SV case in the presence of attenuation. Then, only the SH case can be treated correctly (Trampert *et al.* 1993). The propagator estimation procedure remains valid in a vertically inhomogeneous medium.

The following procedure is used to stabilize the spectral divisions in eqs (33)–(37). For arbitrary signals $F(\omega)$ and $D(\omega)$, the spectral division of $F(\omega)$ by $D(\omega)$ is given by:

$$G(\omega) = \frac{F(\omega)}{D(\omega)}. \tag{38}$$

Unfortunately, spectral division is numerically unstable both because signals are band-limited and due to the existence of low-amplitude notches in the spectrum. In practice, the spectral ratio is estimated using the following technique (Helmberger & Wiggins 1971; Langston 1979):

$$G'(\omega) = \frac{F(\omega)D^*(\omega)}{\Phi_{DD}(\omega)} W(\omega), \tag{39}$$

where

$$\Phi_{DD} = \max\{D(\omega)D^*(\omega), c\max[D(\omega)D^*(\omega)]\}, \tag{40}$$

and $W(\omega)$ is a frequency window to limit the final frequency band in the estimated deconvolution. The complex conjugate of D is denoted by D^*. The function Φ_{DD} can be thought of as simply being the autocorrelation of $D(\omega)$ with any spectral notches filled to a level depending on the parameter c. The frequency windowing function $W(\omega)$ is a tapered window with cut-off frequencies set to the minimum and maximum frequencies for which

$$D(\omega)D^*(\omega) > c\max[D(\omega)D^*(\omega)]. \tag{41}$$

This criterion implies that the parameter c also controls the bandwidth of the spectral ratio $G'(\omega)$.

4 PROPAGATOR INVERSION

4.1 Half-space example

We shall first illustrate the inversion scheme for near-surface velocities with a half-space example. Synthetic data are computed using the Cagniard–de Hoop method (de Hoop & van der Hijden 1983). We restrict ourselves to the *P–SV* case since *SH* was fully treated by Trampert *et al.* (1993). The *P*-wave velocity is 600 m s^{-1}, the *S*-wave velocity is 200 m s^{-1} and the density is 1600 kg m^{-3}. An explosive line source is located at 200 m depth and emits a 120 Hz Ricker wavelet. Multicomponent geophones are positioned at 50 m offset, one is located at the free surface and the second geophone is located at 1.0 m depth (Fig. 5). Fig. 6 shows traces recorded by these receivers.

The propagators P_{11}, P_{13}, P_{31} and P_{33} may be estimated from these data. Theoretical solutions for propagator filters are functions of α, β and p. Fig. 7(a) shows these filters for the given model parameters. Before comparing these propagator coefficients with the data-estimated propagator filters, it is necessary to limit the frequency band of these theoretical expressions to the same frequency band as used for the data-estimated propagator filters. The time domain expressions of the frequency windowing functions $W_{ij}(\omega)$ (eq. 39), where W_{ij} are the frequency windowing functions for propagator components P_{ij}, are shown in Fig. 7(b). Fig. 7(c) illustrates the data-estimated and band-limited theoretical propagators.

We choose to invert the propagator for near-surface velocities in the time domain. In this domain, the propagators can be interpreted as follows. The time delay between the peaks in P_{11} and P_{33} gives the two-way vertical traveltime for *SV* and *P* waves, and the amplitudes of the propagator filters are controlled by the velocity structure between the free surface and depth Δz and the signal bandwidth. To constrain α, β and p from the propagator waveforms, we define the following objective function:

$$E = E_{11} + E_{33} + E_{13} + E_{31}, \tag{42}$$

with

$$E_{ij} = \left(\sum_{t=t_1}^{t_2} [P_{ij}(t, x) - \hat{P}_{ij}(t, x, \alpha, \beta, p)]^2 \right)^{1/2}. \tag{43}$$
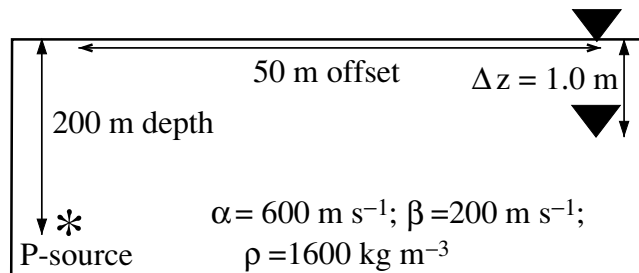
Figure 5. Geophone configuration and parameters of the half-space model.
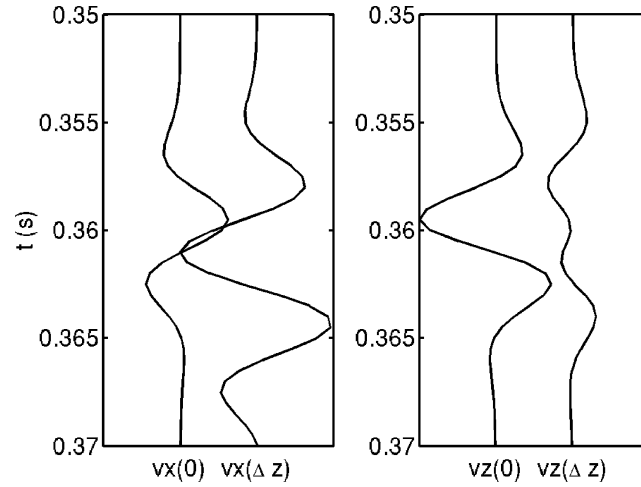
Figure 6. Synthetic traces of the particle velocity recorded by the surface and buried geophone shown in Fig. 5. The left graph shows traces of v_x and the right graph of v_z.
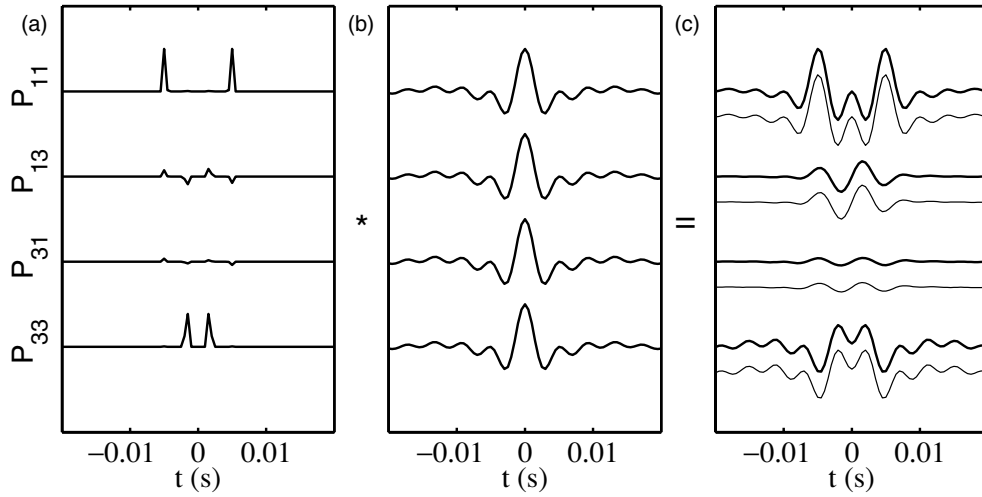

Figure 7. Propagator fitting procedure for the data displayed in Fig. 6. Given estimates for α, β and p, theoretical solutions for the wavefield extrapolation filters can be computed (a). In practice, data are band-limited, and therefore this theoretical solution cannot be compared directly with the estimated filters. (b) The time-domain expressions of frequency filters which limit the solution to the frequency band in which the spectral division was performed. A convolution of the theoretical solution in (a) with the filter shown in (b) allows a comparison with the data-estimated propagator. Part (c) shows that there is a good agreement between the theoretical (thin lines) and data-estimated propagator filters (thick lines). The stabilization factor $c = 1 \times 10^{-3}$.

The theoretical solution for the propagator filter component ij is denoted by $\hat{P}_{ij}(t, x, \alpha, \beta, p)$ and $P_{ij}(t, x)$ is the data-estimated propagator filter component ij. The objective function E is a function in a 3-D model space. Cross-sections of the objective function (Fig. 8) show that perturbations in p have a relatively small influence on estimates of α and β.

So far, we have considered noise-free data. The data-estimated propagator filters for recorded data perturbed by 25 dB uncorrelated Gaussian noise are shown in Fig. 9. These are compared with the theoretical filters for different values of the stabilization factor c (eq. 40), namely $c = 10^{-4}$, $c = 10^{-3}$ and $c = 10^{-2}$. For increasing value of c, the effect of noise is reduced in the propagator filters. Furthermore, the frequency band is more limited for a higher c value. The filters are smoothed and contain less energy.

We estimated the relative variations in α, β and p for different noise levels and c values. To quantify the effect of noise, we define the relative root-mean-square error (RMS) in α by:

$$\text{RMS}(\alpha) = \frac{1}{\alpha_0} \left(\frac{\sum_{i=1}^{N}(\alpha_i - \alpha_0)^2}{N} \right)^{1/2}, \tag{44}$$

with α_0 the model P-wave velocity and α_i the estimated P-wave velocities, which are found by minimizing E in eq. (42). Similar expressions are defined for the relative RMS error in β and p. For each noise level, experiments were conducted 1000 times ($N = 1000$) with different manifestations of Gaussian noise. The minimum of the objective function E was determined using a forward search method. Fig. 10 shows that the estimates of α, β and p are most robust for $c = 10^{-2}$: c clearly stabilizes noise very systematically. Furthermore, α and β are better constrained than p, which implies that relative errors in estimates of p have less influence on estimates of the other parameters than do relative errors of similar magnitude in either α or β.
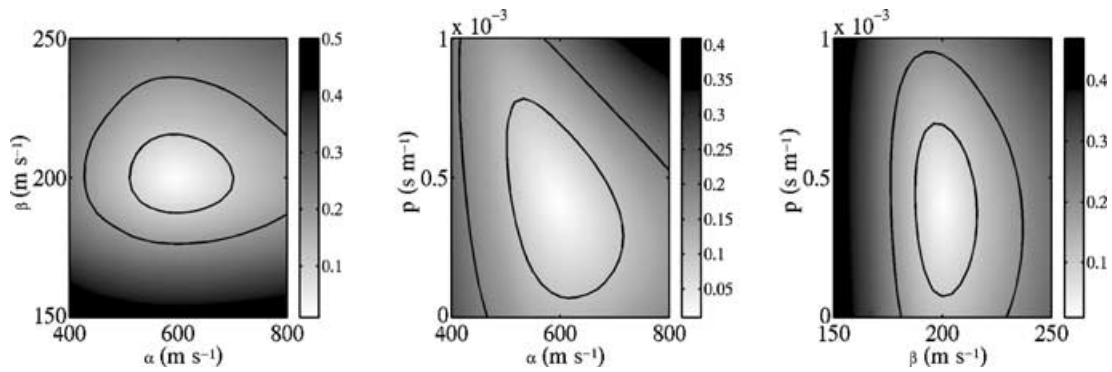
Figure 8. Cross-sections intersecting the minimum of the objective function E. Contours are drawn for $E = 0.10$ and $E = 0.20$.
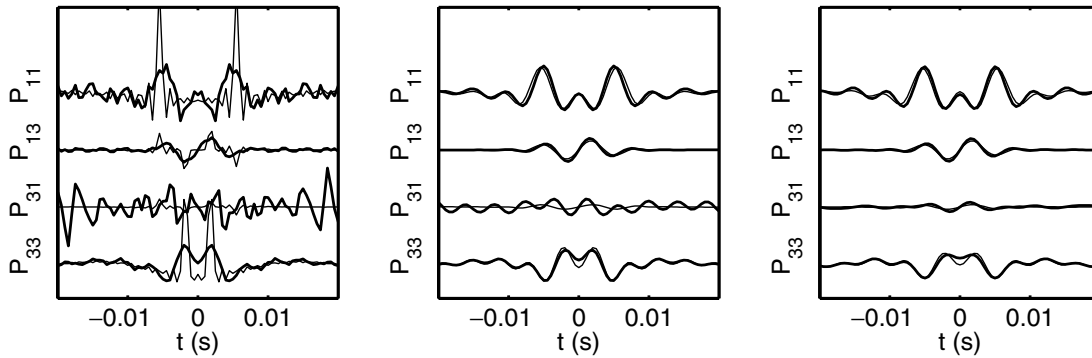

Figure 9. Effect of the stabilization factor c on noise-perturbed propagator filters. The S/N ratio is 25 dB. The propagator filters are computed for $c = 10^{-4}$ (left), $c = 10^{-3}$ (centre) and $c = 10^{-2}$ (right). The thin lines are the band-limited theoretical solutions and the thick lines the data-estimated propagators. The amplitudes of each filter are normalized to the solution for $c = 10^{-4}$. For increasing values of c, the noise is effectively reduced.
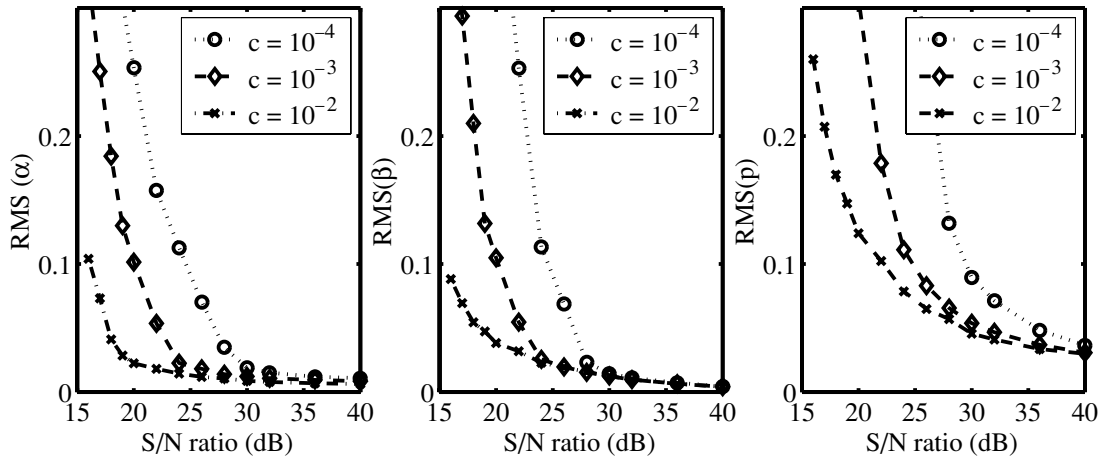

Figure 10. Uncertainties in estimates for α, β and p for different S/N ratios and c values.

In addition to random errors, the effect of position and orientation errors of the geophones within the recording pattern is investigated. We only consider misorientation in the xz-plane, described by rotation angle θ (positive for rotation in clockwise direction). The effects of misorientation and mislocation are quantified with a relative error e. The relative error in α is given by:

$$e(\alpha) = (\alpha - \alpha_0)/\alpha_0. \tag{45}$$

Similar expressions are used for relative errors in β and p. Fig. 11(a) shows the relative error in estimates for α, β and p due to misorientation of the geophone located at the free surface. The errors in α and β are small compared with relative errors in p. Large errors are found for θ close to the angle of incidence. In this example, there are only free-surface incident P waves. This rotation causes the energy on the horizontal recording and thus on the denominator $D(\omega)$ (equation 37) to be minimized. As a consequence, the spectral divisions (eqs 33–36) become
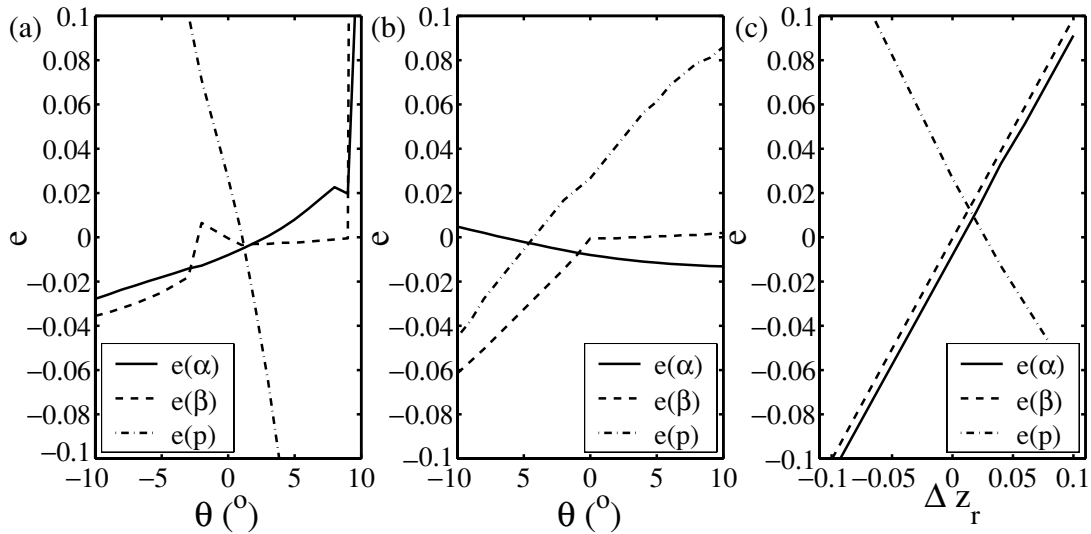
Figure 11. Errors in velocity estimates due to mislocation and misoriention: (a) misorientation in the xz plane of a surface geophone; (b) misorientation in the xz plane of a buried geophone; (c) vertical mislocation of a buried geophone. The stabilization factor $c = 10^{-3}$.

unstable. In the case of near-surface structure, we do not expect such a rapidly increasing error, because in that case both P and S waves will be recorded.

The errors caused by misorientation of the buried geophone is shown in Fig. 11(b). Here, $e(\alpha)$ and $e(\beta)$ remain small, because $\mathbf{v}(\omega, \Delta z)$ does not contribute to the denominator $D(\omega)$. Finally, the effect of vertical mislocation of the buried geophone is illustrated in Fig. 11(c)—the values for Δz are changed in the inversion procedure; the relative change in the depth for the buried geophone $\Delta z_r = (\Delta z - \Delta z_0)/\Delta z_0$, with Δz_0 the true depth of the buried geophone. There is a linear relationship between errors in Δz and estimated velocities. This implies that the phase contains most information on the velocities.

It is difficult to make a fair comparison between wave-equation inversion techniques and propagator inversion. Wave-equation inversion uses the *amplitudes* in the wave equation (eq. 1) to constrain α and β. This requires measurement of spatial and temporal wavefield derivatives by a dense 3-D geophone configuration, with a spatial separation on a subwavelength scale. Propagator inversion, on the other hand, uses mainly *phase* information. To estimate time differences reliably, the depth separation between geophones needs to be larger than those used for wave-equation inversion. Therefore, we used different depths for the buried geophone and different dominant frequencies for the source wavelet.

The obtained results suggest that propagator inversion is less sensitive to both random and deployment related data perturbations. For a S/N ratio of 25 dB, propagator inversion gives no error in α and β, whereas for the wave-equation inversion techniques Figs 3 and 4 indicate more than 20 per cent deviations in estimates for α, while β is still well resolved. Furthermore, Fig. 11 demonstrated that propagator inversion is tolerant to at least $5°$ misorientations and 5 per cent vertical mislocations of individual geophones. Derivative operators on the other hand are particularly sensitive to random misorientations of geophones. Muijs *et al.* (2002) showed that computation of divergence and curl with dense 3-D recording geometries requires that the orientations of all geophones are accurate within $2°$. This criterion needs to be satisfied as well for wave-equation inversion techniques.

Although propagator inversion is tolerant to measurement errors, it is questionable whether this is the dominant source of errors for this method, since a single slowness assumption is implicit in propagator estimation and inversion. Wave-equation inversion techniques do not have this assumption and are applicable to the complete wavefield. In the following experiments, we investigate if propagator inversion is accurate in a model with near-surface structure.

4.2 Low-velocity layer example

The second experiment is performed in a model with a near-surface low-velocity layer. Reverberations in this layer result in multiple arrivals. The near-surface layer is 5 m thick with $\alpha = 600$ m s^{-1}, $\beta = 200$ m s^{-1} and $\rho = 1600$ kg m^{-3}. The parameters of the underlying half-space are: $\alpha = 1500$ m s^{-1}, $\beta = 400$ m s^{-1}, and $\rho = 1800$ kg m^{-3}. The P-source is located at 100 m depth and emits a 120 Hz Ricker wavelet (see Fig. 12). The receiver group is similar to the previous experiment. Synthetic data are computed with a reflectivity method (Kennett 1983). The recorded synthetic traces are shown in Fig. 13. These clearly show the multiple arrivals due to interfering waves in the near-surface low-velocity layer.

The data-estimated propagators are again compared with the theoretical propagators (Fig. 14). The latter were computed for the horizontal slowness of the first break, which is 3.1×10^{-4} s m^{-1}. Due to the multiple arrivals (multiple horizontal slownesses), there is not an exact match between the theoretical and data-estimated propagators. The energy in the propagator filters decays for higher values of c. For too high a c
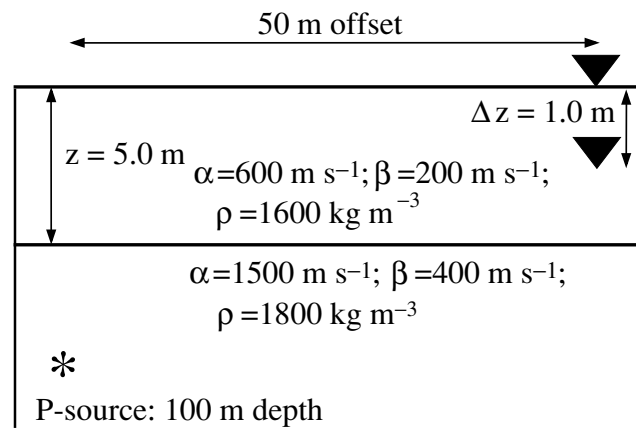
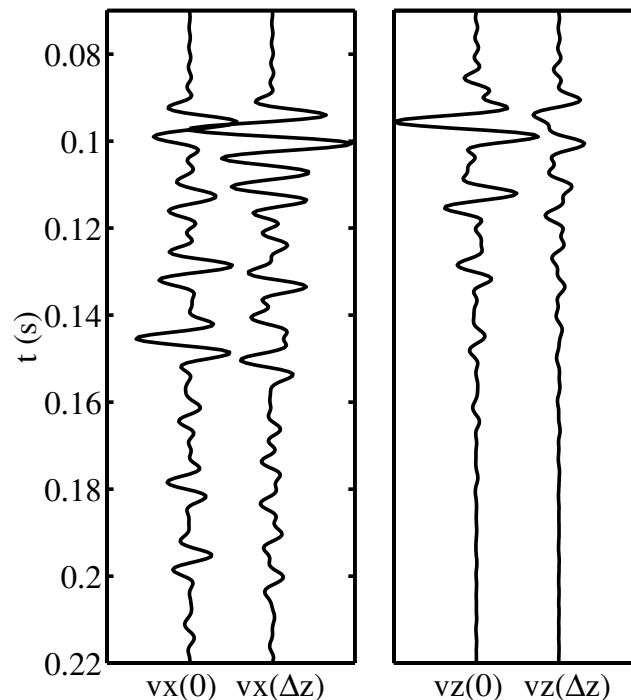**Figure 12.** Model and geophone configuration for experiment with a near-surface low-velocity layer.

Figure 13. Synthetic traces recorded by the geophone configuration displayed in Fig. 12. Recordings of v_x (left) and v_z are shown (right).

value, the fit between the theoretical and data-estimated propagator deteriorates. This can be attributed to the stabilization of internal notches in $D(\omega)$, whereas the theoretical propagator is not compensated for the energy decay in **P** due to this stabilization.

Cross-sections of misfit functions using $c = 10^{-3}$ are shown in Fig. 15. The minimum is located close to the model velocities, whereas the estimated p tends to be smaller than that of the first break, namely around 2.8×10^{-4} s m^{-1}. Waves reverberating in the low-velocity layer arrive at smaller angles of incidence, thus the estimated p can be regarded as some averaged value over all these arrivals.

Fig. 16 illustrates the effects of added noise on velocity and slowness estimation. For high S/N ratios, the estimates for α and β do not exactly converge for $c = 5 \times 10^{-3}$ and $c = 10^{-2}$, as was suggested by Fig. 15 as well. The estimated horizontal slowness differs from that of the direct arrival and varies for different values of c. As in the half-space example, c stabilizes the effects of noise. Reliable estimates for α and β are obtained for S/N ratios down to approximately 18 dB.

4.3 Structure between the surface and the buried geophone

A critical assumption in the propagator inversion scheme is that the medium between the surface and buried geophones is homogeneous. However, according to the classical Hertz–Mindlin model (Mindlin 1949), velocities increase with confining pressure and thus with depth, especially in the top few metres. This also has been observed in field experiments (e.g. Bachrach *et al.* 2000). Here, we consider a model with a large velocity gradient close to the free surface. The velocity gradient decreases with depth (Fig. 17). The gradient model is parametrized by
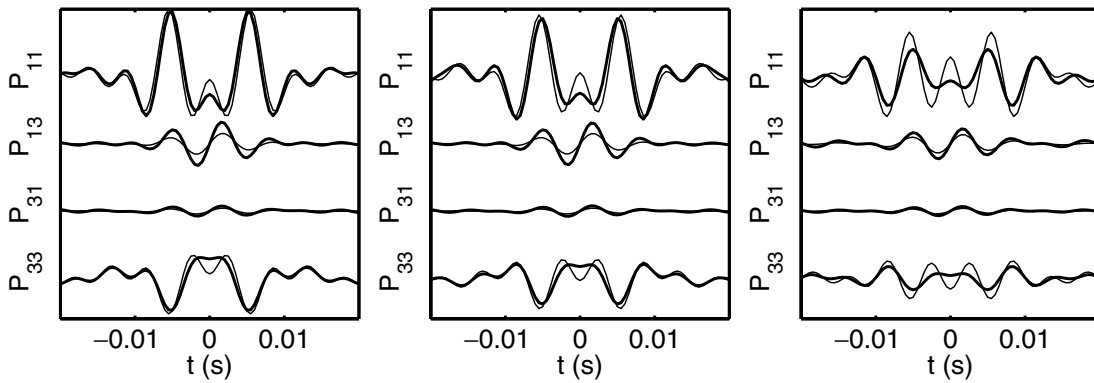
Figure 14. Effect of the stabilization factor c on estimated propagators: $c = 10^{-4}$ (left), $c = 10^{-3}$ (centre) and $c = 10^{-2}$ (right). The thin lines are the theoretical solutions computed with the horizontal slowness of the first break and the thick solid lines are the propagators estimated from the data. Traces are normalized with respect to the $c = 10^{-4}$ curves.
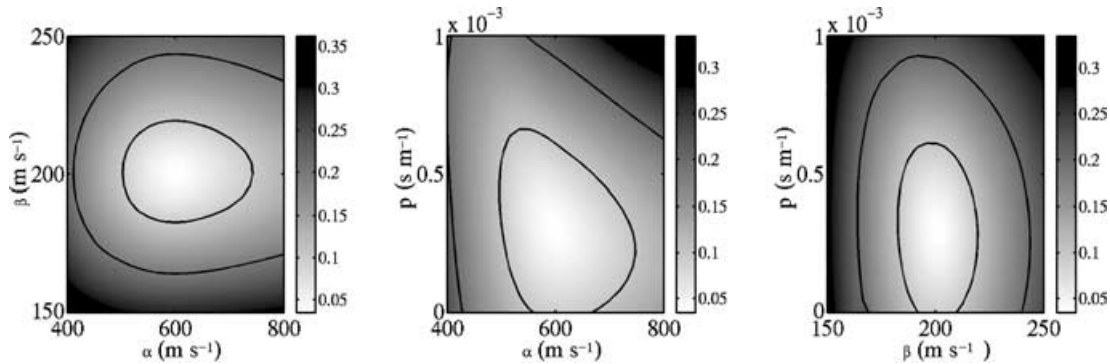

Figure 15. Cross-sections intersecting the minimum of the objective function E for the low-velocity layer model. Contours are drawn for $E = 0.10$ and $E = 0.20$ and $c = 10^{-3}$.
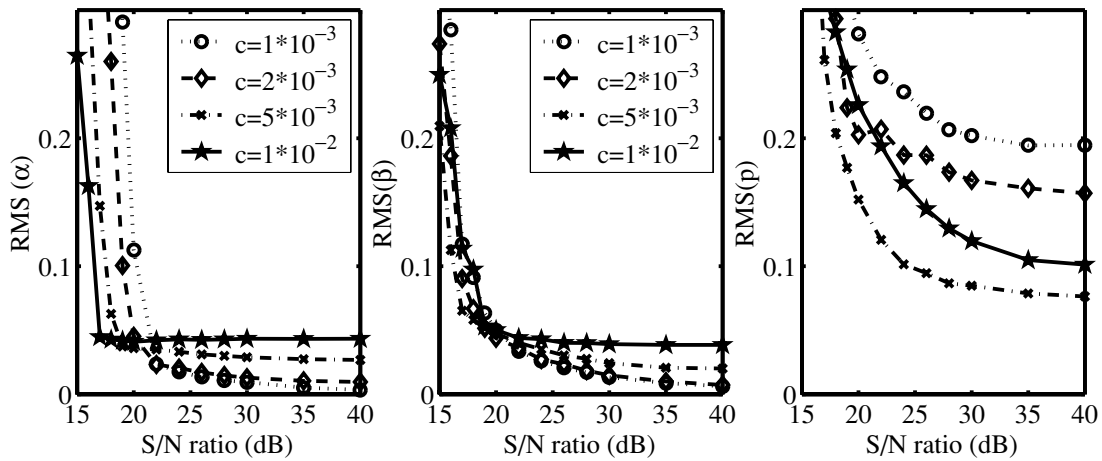

Figure 16. Uncertainty in estimates for α, β and p for different c values as a function of the S/N ratio. The estimated horizontal slowness is compared to the slowness of the direct arrival.

0.02 m thick layers. Synthetic data are computed using a reflectivity method (Kennett 1983). The explosive line source is located at a depth of 100 m and 50 m offset, and emits a 120 Hz Ricker wavelet. The buried geophone is located at a depth of 1.0 m. Fig. 18 shows the synthetic traces for both the surface and buried multicomponent geophones. Data-estimated propagators are shown in Fig. 19. These are compared with theoretical solutions with effective medium velocities, the lower and upper bounds of which are given by the Reuss and Voigt average velocities (Wang & Nur 1992). For the top 1.0 m, the Reuss velocities are $\alpha^- = 259$ m s^{-1} and $\beta^- = 101$ m s^{-1}, and the Voigt velocities are $\alpha^+ = 284$ m s^{-1} and $\beta^+ = 105$ m s^{-1} respectively. The average value of the Voigt and Reuss velocities is used to compute the theoretical propagator. Although the propagator waveforms do not exactly match, the time lags of the peaks are similar. Fig. 20 shows cross-sections of the misfit function. Both α and β are well constrained, whereas p cannot be resolved. The estimated velocities are $\alpha = 272 \pm 8$ m s^{-1} and
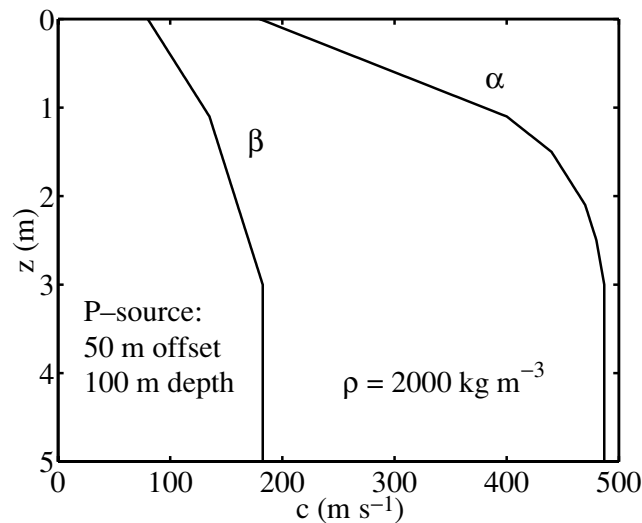
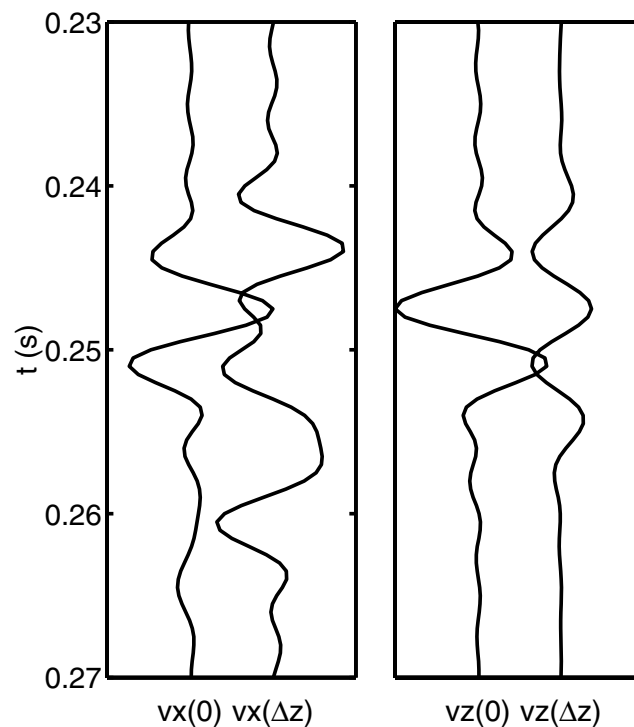**Figure 17.** Gradient velocity model and source location.

Figure 18. Synthetic data recorded in the gradient model at 50 m offset. The buried geophone is located at a depth of 1.0 m and the *P* source at a depth of 100 m.

$\beta = 102.8 \pm 0.6$ m s^{-1}. These values are obtained by performing repeated experiments ($N = 1000$) with different manifestations of random noise (S/N = 25 dB), determining the minimum of the objective function E with a forward search method, and using the average and standard deviation of all these estimates. The obtained velocities fall within the Voigt and Reuss bounds for effective medium velocities.

5 DISCUSSION

Three methods to estimate near-surface properties were evaluated in this paper. The first two methods are based on inversion of the wave equation, whereas the third method inverts wavefield propagator filters for near-surface velocities. A fundamental difference between the methods is that wave-equation inversion schemes use amplitude information to constrain α and β. By changing α and β, the amplitudes in the wave equation change, not the phase. On the other hand, propagator inversion uses predominantly phase information to constrain α and β, i.e. the time lags of the peaks in the propagator coefficients are controlled by the wave velocities.
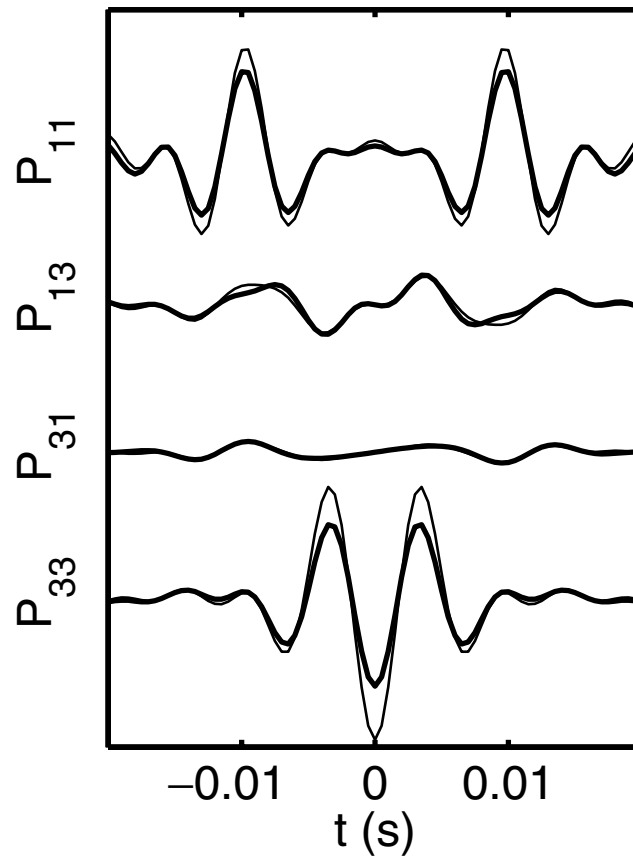
Figure 19. Data-estimated and theoretical propagators in the gradient model. The theoretical propagator is computed using the average value of the Voigt and Reuss effective medium velocities: $\alpha = 272$ m s^{-1} and $\beta = 103$ m s^{-1}, $p = 8.75 \times 10^{-4}$ (s m^{-1}) and $c = 10^{-3}$.
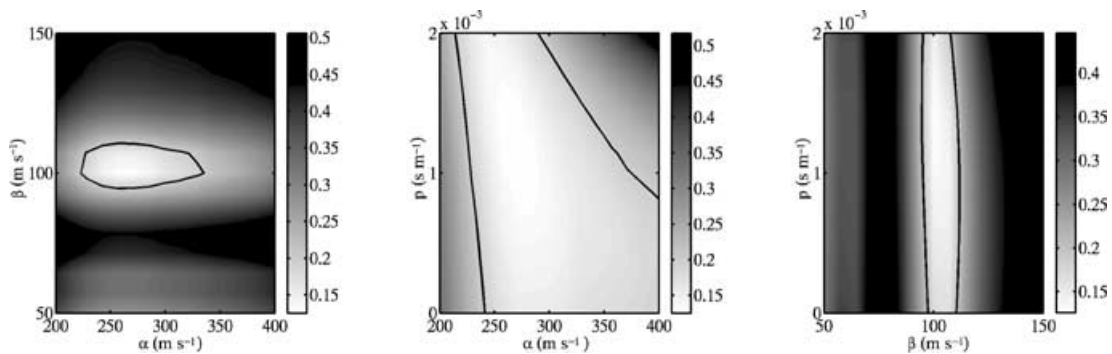

Figure 20. Cross-sections through the minimum of the objective function E for the gradient model. A contour is drawn for $E = 0.20$ and $c = 10^{-3}$.

These sensitivities for either predominantly amplitude information or phase information result in a different optimum experimental set-up. Wave-equation inversion techniques require the measurement of spatial wavefield derivatives, with a spatial geophone spacing on a subwavelength scale. Propagator inversion on the other hand uses mainly phase information. To estimate time differences accurately, both the depth separation of the surface and the buried geophone and the bandwidth of the recorded signal have to be larger. For this reason, we used different configurations, different frequencies and a different depth of the buried geophone, to compare wave-equation inversion techniques with propagator inversion.

Before fitting the waveforms in the wave-equation inversion schemes, either spatial wavefield derivatives or interpolants need to be evaluated. For an accurate implementation of these methods, the spacing between geophones must be sufficiently close, approximately 1/6 of the effective wavelength. Since the wavelength depends on the material properties, some prior knowledge has to be available to design the receiver group.

Propagator inversion on the other hand has no wavelength constraints on the maximum allowed separation of geophones. Therefore, the method may be applicable to borehole recordings. This has been demonstrated for the *SH* case by Trampert *et al.* (1993). However, in

the *P–SV* case we only treated the elastic situation, whereas attenuation has to be included in the formulation for borehole applications. The near-surface velocity estimates presented in this paper are not affected by attenuation, because the geophone separation $\Delta z \ll \lambda$.

However, for a geophone buried at too shallow a depth, propagator inversion cannot resolve the wave velocities. Then, small errors in the phase will cause large uncertainties in the estimated velocities, especially for α. These uncertainties are reduced by increasing the depth of the buried geophone (Van den Berg *et al.* 2003). The minimum depth for the buried geophone depends on the frequency band, the angle of incidence, on α and on the time sampling rate.

The wave-equation inversion schemes use the complete wavefield as input signal. Any event which satisfies the wave equation provides constraints on the near-surface properties. The main sources of error which need to be dealt with are deployment-related errors. Muijs *et al.* (2002) demonstrated that errors such as misorientation and mislocation of individual geophones significantly affect estimates of spatial wavefield derivatives. Correction schemes need to be developed to compensate for these effects. Propagator inversion, on the other hand, avoids the explicit computation of spatial wavefield derivatives. As a consequence, this method is less sensitive to these types of errors.

In contrast to wave-equation inversion techniques, a single slowness assumption is required to construct and invert the propagator filters. As a consequence, those data containing arrivals that are isolated in time need to be selected before this method can be applied. We demonstrated, however, that in a medium with a near-surface low-velocity layer, estimates for α and β are not significantly affected by signal-generated reverberations, and that in a model with a strong velocity gradient, effective medium parameters are obtained.

The following strategies for propagator inversion can be developed by combining data of different shots. First, if the horizontal slownesses in selected data show little variation for different shot points it is possible to reduce effects of noise by stacking the estimated propagator filters. Second, propagator inversion can be formulated without requiring the isolation of an event which can be approximated by a single plane wave. When using a dense source array, the frequency–wavenumber spectra can be computed for common receiver gathers of both the surface geophone and the geophone at depth. Consequently, propagator filters can be determined for each wavenumber or horizontal slowness individually by a spectral division of these two spectra, Thus, propagator inversion is potentially applicable to the complete wavefield. However, difficulties might arise due to lateral variations in near-surface material parameters and poor repeatability of the source.

Synthetic tests have been performed in two dimensions, whereas 3-D wave propagation has to be considered in the field. Applications in the field require a different acquisition geometry for wave-equation inversion. Wave-equation inversion techniques require a 2-D patch of 4×4 receivers at the surface and a buried geophone in the centre at this geophone group. Then, all spatial and temporal derivatives or interpolants can be computed. Propagator inversion requires the separation of *P–SV* waves from *SH* waves, hence rotation of the recordings in the in-line/cross-line direction is required. Furthermore, propagator inversion is aided by an estimate for the horizontal slowness in the in-line direction, and therefore a cross pattern of receivers at the surface is recommended for field applications. The general characteristics of the considered methods do not change in three dimensions, and therefore the presented 2-D synthetic results will apply to the 3-D situation.

6 CONCLUSIONS

We evaluated three methods for estimating local near-receiver material properties. A fundamental difference between the methods is that the wave-equation inversion schemes constrain the *P*-wave and *S*-wave velocities by matching amplitudes in the wave equation, whereas propagator inversion constrains the wave velocities using predominantly phase information, i.e. with the traveltime from the free surface to the depth of the buried geophone. As a consequence, wave-equation and propagator inversion have different optimum receiver configurations. For wave-equation inversion, the configuration needs to be designed to allow the measurement of spatial wavefield derivatives or interpolants, whereas the configuration in propagator inversion must allow a reliable measurement of a phase difference.

Both the derivative and the integral formulation for wave-equation inversion are almost equally sensitive to the effects of measurement errors. If a configuration with more than one buried geophone would have been allowed, an interpolation scheme may be developed which is less sensitive to these type of errors. However, these configurations are not convenient for practical applications, and therefore were not considered.

Propagator inversion has two advantages and one disadvantage over wave-equation inversion schemes. First, instead of a 3-D receiver configuration, only two geophones are required, one positioned at the surface and one buried. Second, this scheme avoids the explicit evaluation of spatial wavefield derivatives or interpolants and therefore it is less sensitive to deployment-related errors. On the other hand, this technique implicitly assumes that a data window containing arrivals with a similar horizontal slowness can be isolated in the recorded data, whereas wave-equation inversion schemes are applicable to nearly complete recordings. Synthetic experiments were performed to assess the consequences of the single slowness assumption in propagator inversion. These experiments demonstrated that the method is robust with respect to signal-generated reverberations, and in the case of a near-surface velocity gradient, results are consistent with effective medium velocities, the upper and lower bounds of which are given by the Voigt and Reuss averaged velocities. Moreover, when using a shot array, propagator inversion could be formulated without the plane wave assumption, and therefore it is potentially applicable to the complete wavefield.

REFERENCES

Aki, K. & Richards, P.G., 2002. *Quantitative Seismology*, 2nd edn, University Science Books, Sausalito, CA, USA.

Aritman, B.C., 2001. Repeatability study of seismic source signatures, *Geophysics,* **66,** 1811–1817.

Bachrach, R., Dvorkin, J. & Nur, A.M., 2000. Seismic velocities and Poisson's ratio of shallow unconsolidated sands, *Geophysics,* **65,** 559–564.

Ben-Menahem, A. & Singh, S.J., 1981. *Seismic Waves and Sources*, Dover, New York.

Curtis, A. & Robertsson, J.O.A., 2002. Volumetric wavefield recording and wave-equation inversion for near-surface material properties, *Geophysics,* **67,** 1602–1611.

Dankbaar, J.W.M., 1985. Separation of P- and S-waves, *Geophys. Prospect.,* **33,** 970–986.

de Hoop, A.T. & van der Hijden, J.H.M.T., 1983. Generation of acoustic waves by an impulsive line source in a fluid/solid configuration with a plane boundary, *J. acoust. Soc. Am.,* **74,** 333–342.

Gao, L., Parker, K.J., Lerner, R.M. & Levinson, S.F., 1996. Imaging of the elastic properties of tissue—a review, *Ultrasound Med. Biol.,* **22,** 959–977.

Goupillaud, P.L., 1961. An approach to inverse filtering of near-surface layer effects from seismic records, *Geophysics,* **26,** 754–760.

Helmberger, D. & Wiggins, R.A., 1971. Upper mantle structure of Midwestern United States, *J. geophys. Res.,* **76,** 3229–3245.

Kähler, S. & Meissner, R., 1983. Radiation and receiver pattern of shear and compressional waves as a function of Poisson ratio, *Geophys. Prospect.,* **31,** 421–435.

Kennett, B.L.N., 1983. *Seismic Wave Propagation in Stratified Media*, Cambridge University Press, Cambridge.

Langston, C.A., 1979. Structure under Mount Rainier, Washington, inferred from teleseismic body waves, *J. geophys. Res.,* **84,** 4749–4762.

Levander, A.R., 1988. Fourth-order finite-difference P–SV seismograms, *Geophysics,* **53,** 1425–1435.

Mindlin, R.D., 1949. Compliance of elastic bodies in contact, *J. Appl. Mech.,* **16,** 259–268.

Muijs, R., Holliger, K. & Robertsson, J.O.A., 2002. Perturbation analysis of an explicit wavefield separation scheme for P- and S-waves, *Geophysics,* **67,** 1972–1982.

Muthupillai, R., Lomas, D.J., Rossman, P.J., Greenleaf, J.F., Manduca, A. & Ehman, R.L., 1995. Magnetic resonance elastography by direct visualization of propagating acoustic strain waves, *Science,* **269,** 1854–1857.

Oliphant, T., Mahowald, J.L., Ehman, R.L. & Greenleaf, J.F., 1999. Complex—valued quantitative stiffness estimation using dynamic displacement measurements and local inversion of conservation of momentum, *IEEE Ultrasonics Symp.,* Vol. 2, 1641–1644.

Oliphant, T.E., Manduca, A., Ehman, R.L. & Greenleaf, J.F., 2001. Complex-valued stiffness reconstruction for magnetic resonance elastography by algebraic inversion of the differential equation, *Magn. Reson. Med.,* **45,** 299–310.

Osen, A., Amundsen, L. & Reitan, A., 1999. Removal of water-layer multiples from multicomponent sea-bottom data, *Geophysics,* **64,** 838–851.

Robertsson, J.O.A. & Muyzert, E., 1999. Wavefield separation using a volume distribution of three component recordings, *Geophys. Res. Lett.,* **26,** 2821–2824.

Romano, A., Bucaro, J.A., Ehman, R.L. & Shirron, J.J., 2000. Evaluation of a material parameter extraction algorithm using MRI-based displacement measurements, *IEEE Trans. Ultrason. Ferroelectr. Freq. Control,* **47,** 1575–1581.

Romano, A.J., Shirron, J.J. & Bucaro, J.A., 1998. On the noninvasive determination of material parameters from a knowledge of elastic displacements: theory and numerical simulation, *IEEE Trans. Ultrason. Ferroelectr. Freq. Control,* **45,** 751–759.

Toksöz, M.N., Cheng, C.H. & Timur, A., 1976. Velocities of seismic waves in porous rocks, *Geophysics,* **41,** 621–645.

Trampert, J., Cara, M. & Frogneux, M., 1993. SH propagator matrix and Q_s estimates from borehole- and surface- recorded earthquake data, *Geophys. J. Int.,* **112,** 290–299.

Unser, M., 1999. Splines, a perfect fit for signal and image processing, *IEEE Signal Process. Mag.,* **16**(6),22–38.

Van den Berg, J., Curtis, A. & Trampert, J., 2003. Optimal nonlinear Bayesian experimental design: an application to amplitude versus offset experiments, *Geophys. J. Int.,* **155,** 411–421.

Van Houten, E.E.W., Paulsen, K.D., Miga, M.I., Kennedy, F.E. & Weaver, J.B., 1999. An overlapping subzone technique for MR-based elastic property reconstruction, *Magn. Reson. Med.,* **42,** 779–786.

Wang, Z. & Nur, A., 1992. *Seismic and Acoustic Velocities in Reservoir Rocks, vol. 2, Theoretical and Model Studies*, Geophysics Reprint Series no 10, Society of Exploration Geophysicists, Tulsa, OK, USA.

Wapenaar, C.P.A., Herrmann, P., Verschuur, D.J. & Berkhout, A.J., 1990. Decomposition of multicomponent seismic data into primary P- and S-wave responses, *Geophys. Prospect.*, **38,** 633–661.

APPENDIX A: COEFFICIENTS FOR DIRECT WAVE-EQUATION INVERSION

The measurable coefficients in eqs (6)–(8) for direct wave-equation inversion are found by inserting the free-surface derivative conditions, eqs (3)–(5), into the wave eq. (1):

$$A_1(t) = \frac{2}{\Delta z}(\partial_1 v_3 + \partial_3 v_1) + \nabla_H^2 v_1 + 2\partial_1(\nabla_H \cdot \mathbf{v}_H), \tag{A1}$$

$$A_2(t) = \frac{2}{\Delta z}(\partial_2 v_3 + \partial_3 v_2) + \nabla_H^2 v_2 + 2\partial_2(\nabla_H \cdot \mathbf{v}_H), \tag{A2}$$

$$A_3(t) = \frac{2}{\Delta z}(\nabla_H \cdot \mathbf{v}_H + \partial_3 v_3) - \nabla_H^2 v_3, \tag{A3}$$

$$B_1(t) = 2\partial_1(\nabla_H \cdot \mathbf{v}_H), \tag{A4}$$

$$B_2(t) = 2\partial_2(\nabla_H \cdot \mathbf{v}_H), \tag{A5}$$

and

$$B_3(t) = \frac{4}{\Delta z}(\nabla_H \cdot \mathbf{v}_H) - 2\left(\nabla_H^2 v_3\right). \tag{A6}$$

The finite-difference (FD) first-order derivatives in depth are denoted $\partial_3 \mathbf{v}$ and are given by:

$$\partial_3 \mathbf{v}(\Delta z/2) = \frac{\mathbf{v}(\Delta z) - \mathbf{v}(0)}{\Delta z} + O(\Delta z^2), \tag{A7}$$

with Δz the depth beneath the free surface of the buried geophone. The vertical derivative cannot be measured exactly at the free surface but at depth $\Delta z/2$. The following notation is used for horizontal wavefield derivatives:

$$\nabla_H = [\partial_1 \quad \partial_2]^{\mathrm{T}}, \tag{A8}$$

and

$$\mathbf{v}_H = [v_1 \quad v_2]^{\mathrm{T}} \tag{A9}$$

Temporal and spatial wavefield derivatives are computed using finite-difference operators.

APPENDIX B: INTEGRAL EQUATION FORMULATION

We demonstrate that the wave eq. (1) can be transformed into an integral equation. Let $\mathbf{w} = (w_1, w_2, w_3)^{\mathrm{T}}$ be a sufficient smooth vector-valued function and Ω a volume bounded by a surface Γ. If the wave equation is multiplied by $\mathbf{w}$ and integrated over the volume Ω, the result is:

$$\int_\Omega \mathbf{w} \cdot \ddot{\mathbf{v}} d\Omega = \int_\Omega \mathbf{w} \cdot [\alpha^2 \nabla(\nabla \cdot \mathbf{v}) - \beta^2 \nabla \times (\nabla \times \mathbf{v})] d\Omega. \tag{B1}$$

The first term of the right-hand side of eq. (B1) can be expanded by repeated application of the divergence theorem:

$$\int_\Omega d\Omega \mathbf{w} \cdot [\nabla(\nabla \cdot \mathbf{v})] = \int_\Gamma d\Gamma [\mathbf{w}(\nabla \cdot \mathbf{v})] \cdot \mathbf{n} - \int_\Omega d\Omega (\nabla \cdot \mathbf{w})(\nabla \cdot \mathbf{v})$$

$$= \int_\Gamma d\Gamma [\mathbf{w}(\nabla \cdot \mathbf{v}) - \mathbf{v}(\nabla \cdot \mathbf{w})] \cdot \mathbf{n} + \int_\Omega d\Omega \mathbf{v} \cdot [\nabla(\nabla \cdot \mathbf{w})], \tag{B2}$$

where $\mathbf{n}$ is the outward-pointing normal vector on Γ. The second term is expanded using the identity,

$$\nabla \times (\nabla \times \mathbf{v}) = \nabla(\nabla \cdot \mathbf{v}) - \nabla^2 \mathbf{v} \tag{B3}$$

and the divergence theorem:

$$\int_\Omega d\Omega \mathbf{w} \cdot [\nabla \times (\nabla \times \mathbf{v})] = \int_\Gamma d\Gamma [\mathbf{w}(\nabla \cdot \mathbf{v}) - \mathbf{v}(\nabla \cdot \mathbf{w}) - \mathbf{w} \cdot (\nabla \mathbf{v})^{\mathrm{T}} + \mathbf{v} \cdot (\nabla \mathbf{w})^{\mathrm{T}}] \cdot \mathbf{n}$$

$$+ \int_\Omega d\Omega \mathbf{v} \cdot [\nabla \times (\nabla \times \mathbf{w})] d\Omega. \tag{B4}$$

In the volume integrals, all spatial wavefield derivatives have disappeared in eq. (B4). Because the vector-valued functions $\mathbf{w}$ can be chosen arbitrarily, boundary conditions can be imposed such that the surface integrals vanish. Consequently, all spatial wavefield derivatives can be made to disappear.